Insight on TiO_2-ZnO Photocomposite Competence Fabricated via Sonication Assisted with Gelatin for Rhodamine B Degradation

Arafat Toghan[1,2]*, Kamal K. Taha[3], A. Modwi[4]*

[1]*Chemistry Department, Faculty of Science, South Valley University, Qena, 83523, Egypt*
[2]*Chemistry Department, College of Science, Imam Mohammad Ibn Saud Islamic University (IMSIU), Riyadh 11623, Saudi Arabia*
[3]*Bahri University, College of Applied & Industrial Sciences, Chemical & Industrial Chemistry Department, Khartoum, Sudan*
[4]*Department of Chemistry, College of Science and Arts at Al-Rass, Qassim University, Saudi Arabia*

Abstract:

Herewith we report a facile synthesis of zinc oxide doped with (5, 10, 15, and 20 wt%) titanium oxide nanocomposites in gelatin under ultra-sonication. The X-ray diffraction (XRD) data revealed ZnO the formation in addition to a rutile phase TiO_2. The ZnO phase size decreased, and the rutile TiO_2 phase increased with a TiO_2 loading increment. The scanning electron microscopy (SEM) displayed a combination of spherical and hexagonal particles with a 60 – 80 nm size distribution. The prepared nanostructures photocatalytic activity was assisted using Rhodamine B dye, where they showed enhanced photodegradation competence under visible light irradiation. The kinetics of photodegradation followed the first-order kinetics with the 20 % wt sample having the maximum activity. The mechanistic investigation revealed the dominance of h^+ and $\bullet O_2^-$ species during the dye photodegradation. The results indicate the potential application of such gelatin stabilized nanostructures for dye illumination from aqueous solutions under sunlight.

Keywords: *TiO_2-ZnO photocatalysts; gelatin; William-Hall plots; Rhodamine B degradation*

*Corresponding authors E-mail addresses: (Arafat Toghan): arafat.toghan@yahoo.com; (A. Modwi): abuelizkh81@gmail.com

Preprints (www.preprints.org) | NOT PEER-REVIEWED | Posted: 1 October 2020 doi:10.20944/preprints202010.0026.v1

1. Introduction

Polymer stabilized nanocomposites are recently becoming of prime research interests by virtue of their value added benefits such as improved stabilizing, fictionalization, magnetic, thermal and mechanical qualities [1-3]. Being abundant, hydrophilic, biocompatible and biodegradable natural biopolymers are favored over the synthetic [4]. Gelatin obtained by denaturation of collagen is formed of a single sequence of amino acids. It is warm water soluble and gels when its concentration exceeds 1wt% [2]. It has the ability to coordinate with metal ions due to the polar groups in its structure [5]. Gelatin was dissolved in the sol form and used as a structure-guiding agent to tailor the ZnO nanostructures morphology. For instance, ZnO nano-plates were developed from ZnO nanoparticles using gelatin [6], while Bauermann *et al*. fabricated hexagonal ZnO plates in a gelatin matrix [5]. Gelatin was employed to stabilize CdTe/CdS/ZnS (CSSG) core/double shell quantum dots (QDs) to advance their biocompatibility[7], copper NPs [8] and ZnO NPs [9].

The n-type and large band gap semiconductors like ZnO, TiO_2, and SnO_2 have triggered the researchers curiosity persuading them to explore their properties and applications [10]. To benefit from the ZnO flexibility in synthesis and morphologies and the stability of TiO_2,acouplingof TiO_2 and ZnO nanoparticles is a convenient approach to induce substantial effects on the morphologies, porosity, electronic, and photo-electrochemical characteristics [11]. The catalytic activity of TiO_2 was enhanced by adding ZnO [12] where the electron and hole transfer between their conduction and valence bands leads to a well separation of photogenerated charge carriers [12,13]. Previous reported methods of ZnO-TiO_2nanostructures synthesis included magnetron sputtering [14,15], powders thermal processing [16], sol-gel [17,18], chemical vapor deposition [19] and homogeneous hydrolysis [20].

Preprints (www.preprints.org) | NOT PEER-REVIEWED | Posted: 1 October 2020 doi:10.20944/preprints202010.0026.v1

In this study different gelatin stabilized TiO_2 doped ZnO nanocomposites were synthesized via ultrasonic energy. A titanium oxide rutile phase has immerged and the morphology has altered as a result of doping. The optical properties and the employment of the nanocomposites to decolorize the RhB dye were investigated and the kinetics and mechanism of the process were probed.

2. Experimental methods

2.1. Preparation of TiO_2-ZnO photocomposites

For the synthesis of TiO_2-ZnO photocomposites at different TiO_2 nanoparticles content (5, 10, 15 and 20 wt%), gelatin and ultra-sonication process is employed. The required amounts of TiO_2 and fixed amount of ZnO nanoparticles were dispersed in 100ml of absolute ethanol and the mixture sonicated at room temperature for 30min until the milky solution formed. The mixture obtained was added gradually to the 100ml of a hot solution of gelatin under vigorous stirring. Next, the mixture is sonicated for 1h at 50^{o}C and dried in an oven at 120^{o}C for 6h. The dried samples were calcined at 650 C in air atmosphere for an hour using muffle furnace. The samples were labelled as (5%ZnO, 10%ZnO, 15%ZnO, and 20%ZnO).

2.2. Characterization of the photocomposites

The crystalline structure of the powders was investigated by X-ray powder diffraction (XRD) using Bruker high-resolution diffractometer equipped with Cu-Ka radiation (1.5418 Å), operating at 40 kV and 40 mA. Morphological images recorded by field emission scanning electron microscopy (FE-SEM) using high-resolution Jeol JSM 7600F. The optical properties were determined by means of diffuse reflectance spectroscopy (DRS) using JASECO V-770 spectrophotometer in the wavelength range 300-800 nm.

Preprints (www.preprints.org) | NOT PEER-REVIEWED | Posted: 1 October 2020 doi:10.20944/preprints202010.0026.v1

2.3. Photocatalytic efficacy of fabricated photocatalysts

The photocatalytic competence of the as-fabricated photocomposites was assessed by monitoring the photodegradation of Rhodamine B dye under visible-light illumination. In a typical test, 50 mg the photocatalyst powder was dispersed in 100 ml aqueous solution of RhB dye concentration = 20 mg L^{-1}. Prior to the light illumination, the photocatalyst with the dye solution was strongly magnetically stirred (400 rotation/min) in full darkness for 30min under the ambient condition to achieve an adsorption/desorption equilibrium of dye on the photocatalyst surface. Then 5 ml of the mixture solution was withdrawn as an initial concentration (C_o) and exposed to visible-light irradiation (OSRAM lamp 58 IM/W). Following exposure to visible-light 5 ml suspension was withdrawn at different time intervals, centrifuged (5000 rpm for 10 min) to remove suspended and the absorbance was measured. Temporal concentration variations of RhB were measured via the change in the maximal spectra (λ_{max} = 525 nm) of the dye.

2.4. Radicals scavenger experiment

To probe the photocatalytic mechanistic activity of the photocomposites, the effective reactive species (holes and radicals) were identified using radical scavenging tests method. In this method, the valence band holes (h^+), conduction band electrons (e^-), hydroxyl radical ($^*OH$), and super-oxide radical ($^*O_2^-$) were monitored by adding EDTA (h^+) [21], silver nitrate (e^-) [22], isopropanol ($^*OH$) [21], and ascorbic acid ($^*O_2^-$) [22] to the reaction solution, individually, through the process of photocatalytic degradation of RhB dye. In a typical procedure, 50 mg of x% ZnO and 10 mM of radical scavengers were placed in 100 mL of 20 mg. L^{-1} RhB dye solution; then the mixture was illuminated utilizing the visible light at the same time after adsorption equilibrium. Ultimately, the degradation rate of the dye was calculated to highlight the main role of active species.

Preprints (www.preprints.org) | NOT PEER-REVIEWED | Posted: 1 October 2020 doi:10.20944/preprints202010.0026.v1

3. Results and discussion

3.1 XRD analysis

The XRD patterns of the TiO_2/ZnO composite are sketched in Fig. 1. reveal sharp and distinct diffraction peaks with relative intensity and broadening, as a clue of the development of nano-crystalline structure of high crystallinity [23]. The peaks at 2θ = 31, 34, 36, 47, 56, 62, 66, 68 and 69^0 that can be assigned to the (100), (002), (101), (102),(110), (103), (200), (112), (201), (004) and (202) planes of the wurtzite hexagonal ZnO structure in accordance with JCPDS card No. 36-1451, can be observed. In addition extra peaks corresponding to 2θ = 28, 35, 42, 53 and 62^0 delineating the (110), (101), (200), (211) and (310) planes of the TiO_2 rutile phase in agreement with (JCPDS 21-1276) [24-26]. It can be noticed that the intensities of the peaks corresponding to the rutile phase increase proportional to the TiO_2 ratio in the sample (Fig. 1b) which is an expected consequence of the ZnO % lowering in the precursor powders [27]. A noticeable decrease in the FWHM with increase of Ti loading is an indication of improved crystallinity [28]. The Scherrer equation [29] was used to compute the crystallite size of the nanocomposites:

$$D = \frac{0.9\lambda}{\beta cos\theta} \qquad (1)$$

where β is the full width at half maximum (FWHM) of the XRD peak (in radians), the constant, k value of ≈ 0.90, θ is diffraction angle and λ is the wavelength of the Cu-Kα (1.5418 Å). The crystallite size for ZnO wurtzite was estimated taking the most intense peak (101), while the peak (110) was used for the TiO_2 rutile phase. The crystallite size of the wurtzite ZnO *(D(w))* exhibits a decrease with the addition of more TiO_2 [30], while a reverse trend is shown by the rutile phase crystallite size (**D*(*R*)**). From the XRD findings, a successful synthesis of nanocomposites comprising of rutile TiO_2 and wurtzite ZnO can be confirmed. The d-spacing, lattice parameters and the unit cell volumes were estimated by the expressions:

Preprints (www.preprints.org) | NOT PEER-REVIEWED | Posted: 1 October 2020 doi:10.20944/preprints202010.0026.v1

$$d = \frac{\lambda}{2\sin\theta} \quad (2)$$

$$a = \frac{\lambda}{\sqrt{3}sin\theta} and c = \frac{\lambda}{\sin\theta} \quad (3)$$

$$V = 0.866 \times a^2 \times c \quad (4)$$

The micro-strain is estimated via the expression [31] and the stress σ(GPa) in the crystallite's plane [32] are computed

$$\varepsilon = \frac{\beta}{4\,tan\theta} \quad (5)$$

$$\sigma = 233\left(\frac{c_{bulk}-c}{c_{bulk}}\right) \quad (6)$$

where c and c_{bulk} are the measured lattice parameter and the strain-free lattice parameter of ZnO (5.2061 Å) respectively. The Zn – O bond length (L) was calculated using the equation:

$$L = \sqrt{\left[\frac{a^2}{3} + (0.5-u)^2 * c^2\right]} \quad (7)$$

where $u = \frac{a^2}{3c^2} + 0.25$

The tabulated values (Table 1) of the d-spacing, a, c, V and L reveal a decrease with the increment of titanium in the nanocomposites. This may attributed to the substitution of larger radius Zn^{2+} (74 *pm*) by the smaller radius Ti^{4+} (68 pm) [30]. The stress (σ) in the nanocomposites can be estimated by the strain model σ (Gpa) = -233*(c_0 – c)/c_0, where c and c_0 are the lattice constants calculated from XRD data the lattice constant of the pure ZnO (0.5206 nm) respectively [33]. It is evident that the samples containing titania have a negative or very less stress that points to a compressive stress. Thus the minor shrinkage in the lattice parameters can be ascribed to a compressive stress as a result of the partial displacement of the large Zn^{2+} by the small Ti^{4+} in the structures [34,35]. Using the formula ε = β / 4 tan θ, the microstrain (ε) was calculated and tabulated (Table 2). As can be noticed that the microstrain decreased monotonously with the increase in titnia loading

Preprints (www.preprints.org) | NOT PEER-REVIEWED | Posted: 1 October 2020 doi:10.20944/preprints202010.0026.v1

which may be attributed to the atom diffusion [36] during the Ti^{4+} substitution of Zn^{2+} during composites formation. From the table it is evident that the preferred orientation has changed from (002) to the (101) plane as titanium loading is increased as reflected by the increase in (I_{101}/I_{002}) ratio. This may be attributed effect of Zn and Ti atoms that reduce the surface free energy of the (101) which might have changed the plane of minimum surface free energy from (002) to (101) [37].

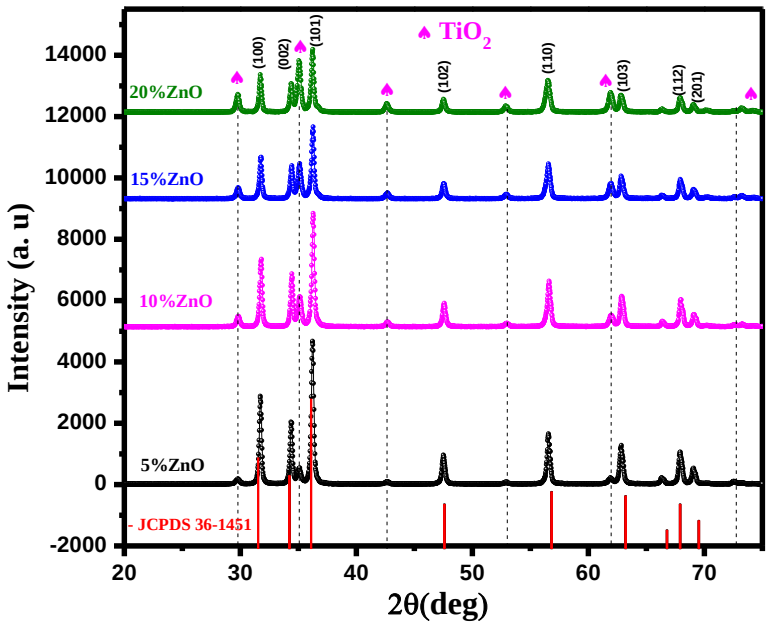

Fig. 1a: XRD patterns of the prepared composites

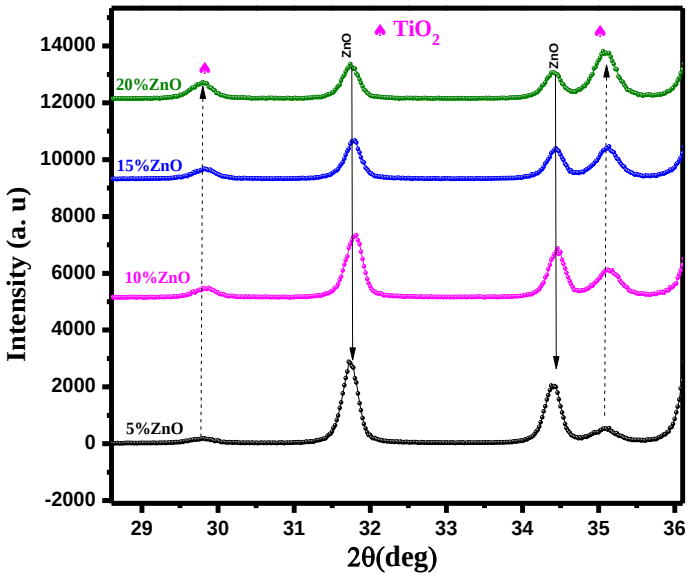

Fig. 1b: Change of TiO_2 and ZnO peaks intensities with the TiO_2 percentage

A logarithmic form of the Scherrer equation is presented in the formula [38]:

Preprints (www.preprints.org) | NOT PEER-REVIEWED | Posted: 1 October 2020 doi:10.20944/preprints202010.0026.v1

$$ln\beta = ln\frac{k\lambda}{D} + ln\frac{1}{cos\theta} \quad (8)$$

The crystallite is calculated from the intercept of lnβ versus ln (1/cosθ) graph. Fig. 2a shows the modified Scherrer equation plots for all of the samples and the calculated values of crystallite size (*D****)* are listed in Table 1. The values are almost equal to those obtained Scherrer equation (equation 1). The slight divergence may be ascribed to the averaging of the distribution considered in the modified Scherrer's plots where the XRD entire peaks are involved [39].

Table 1: Structural parameters of the nanocomposites

Samples	β	2θ (0)	D (w) (nm)	D*(r)(nm)	Lattice parameter (Å) (a)	(c)	I_{101}/I_{002}	ϭ (x10-3) Gpa	ε(x10-3)	D (nm)	V	u	L
5 %ZnO	0.2317	36.232	42.80	25.0	3.253	5.210	0.268	1.78	3.08	2.4768	47.74	0.3799	1.9796
10 %ZnO	0.2231	36.285	37.49	28.38	3.248	5.202	0.555	-2.55	3.00	2.4741	47.52	0.3799	1.9757
15 %ZnO	0.2202	36.262	37.98	28.87	3.249	5.205	1.044	-0.44	2.93	2.4741	47.58	0.3799	1.9772
20 %ZnO	0.2183	36.235	37.31	28.53	3.252	5.208	1.805	0.89	2.91	2.4755	47.69	0.3799	1.9790

3.1.2.Williamson–Hall (W–H) methods for estimation of microstrain (ε) and crystallite size (D):

3.1.2.1. Uniform deformation model (UDM):

According to Williamson–Hall approach [39], strain and crystallite size contribute significantly to the diffraction lines broadening (equation 9) [40,41]. In the uniform deformation model (*UDM*), it is assumed that a crystal is isotropic [42] and subsequently its properties are independent of the crystallographic direction along which the measurement is considered.

$$\beta_{hkl}\cos\theta_{hkl} = \frac{k\lambda}{D} + 4\varepsilon\sin\theta_{hkl} \quad (9)$$

Preprints (www.preprints.org) | NOT PEER-REVIEWED | Posted: 1 October 2020 doi:10.20944/preprints202010.0026.v1

A plot of $\beta_{hkl} \cos\theta_{hkl}$ versus $4 \sin\theta_{hkl}$represents a linear graph [42], and the crystallite size (D) and microstrain (ε) are respectively calculated from the intercept and slope of the line (Fig. 2b).The data obtained are enumerated in table (2).

3.1.2.2. Uniform stress deformation model (USDM):

As isotropy and homogeneity conjecture is unachieved at all instances, a more realistic anisotropic model is therefore developed. Thus, Williamson– Hall formula is reformed by including an anisotropic term related to strain (ε) [43]. In the Uniform Stress Deformation Model (USDM), Hooke's law represents the strain in addition to a direct correlation between the stress (σ), anisotropic microstrain (ε) and Young's modulus (Y_{hkl}) as represented by $\sigma = \varepsilon Y_{hkl}$. For hexagonal ZnO structure (Y_{hkl}) was given as 127GPa [40]. Consequently, the Williamson–Hall formula is remodeled to (10):

$$\beta_{hkl} \cos\theta_{hkl} = \frac{k\lambda}{D} + \frac{4\sigma \sin\theta_{hkl}}{Y_{hkl}} \qquad (10)$$

By plotting $\beta_{hkl} \cos\theta_{hkl}$ as a function of $\frac{4\sigma \sin\theta_{hkl}}{Y_{hkl}}$, σ and D are obtained from the slope and intercept respectively, while ε is computed using Young's modulus, Y_{hkl}, of ZnO nanoparticles hexagon. Fig. (2c) illustrates the *USDM* for the samples and the data obtained is shown (Table 2).

3.1.2.3. Uniform deformation energy density model (UDEDM):

An additional form of Williamson– Hall methods known as the Uniform Deformation Energy Density Model (UDEDM) is applied to deduce the crystal's energy density (u_{ed}). For elastic systems that comply with Hooke's law, u_{ed} is inter related with the strain through the term$u_{ed} = (\varepsilon^2 Y_{hkl})/2$ [40]. Equation (11) provides the *UDEDM* term:

$$\beta_{hkl} \cos\theta_{hkl} = \left(\frac{k\lambda}{D}\right) + \left(4 \sin\theta_{hkl} \left(\frac{2u_{ed}}{Y_{hkl}}\right)^{0.5}\right) \qquad (11)$$

Where $\left(\frac{2}{Y_{hkl}}\right)^{0.5} = 0.1255$

Preprints (www.preprints.org) | NOT PEER-REVIEWED | Posted: 1 October 2020 doi:10.20944/preprints202010.0026.v1

After Plotting $\beta_{hkl} \cos\theta_{hkl}$ versus $4 \sin\theta_{hkl} \left(\frac{2u_{ed}}{Y_{hkl}}\right)^{0.5}$, we can estimate the anisotropic energy density (u_{ed}) from the slope. While, the stress (σ) and microstrain (ε) are estimated from (u_{ed})and Y_{hkl}, and the crystallite size (D) is calculated from intercept [40]. Fig. (2d) displays the USDM for the samples and the results obtained are listed in Table 2.

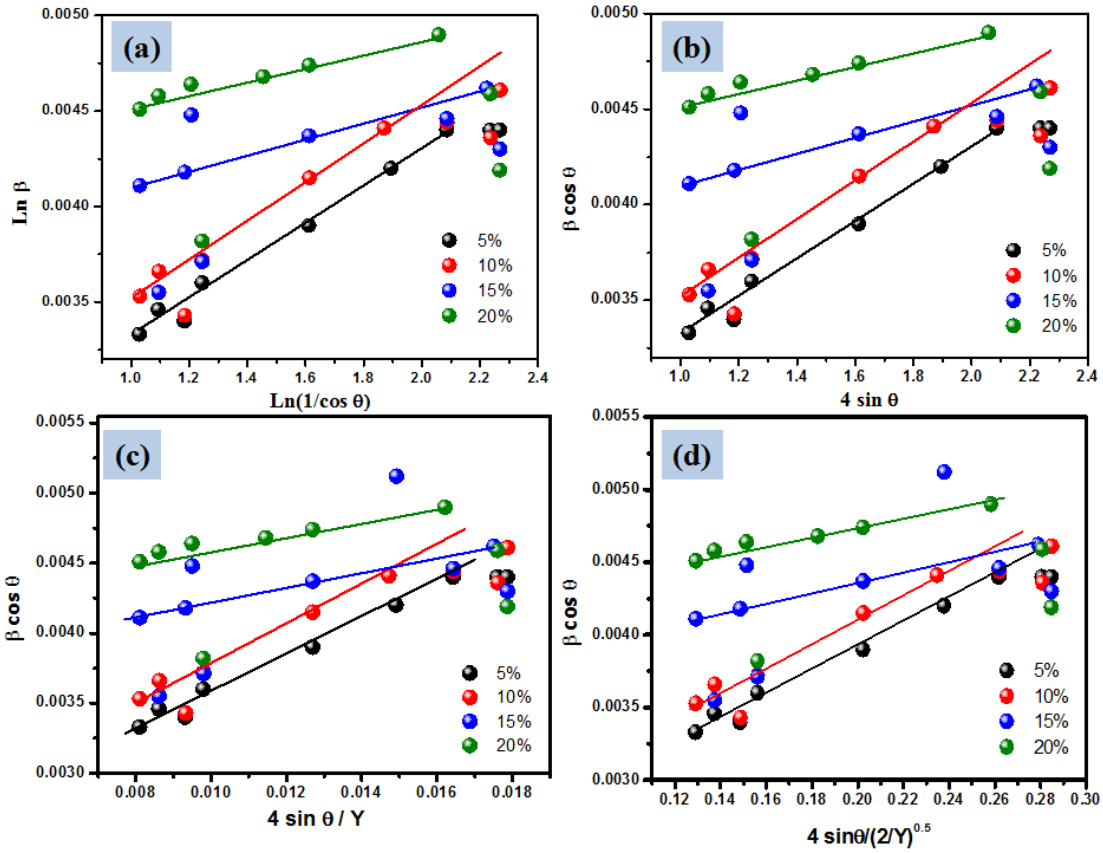

Fig. 3: Scherrer plots (a) and W-H**:** UDM(a), USDM (b) and UDEDM (c)of samples

Table 2: The modified Scherrer and William-Hall plots data of the nanocomposites

Sample	Scherrer D (nm)	Scherrer D* (nm)	Williamson- Hall method								
			UDM		USDM			UDEDM			
			D (nm)	ε x 10^{-4}	D (nm)	ε x 10^{-4}	σ (MPa)	D (nm)	ε x 10^{-4}	σ(MPa)	u_{ed} (KJm^{-3})
5%ZnO	42.80	36.63	57.77	9.0	57.77	9.0	114.4	57.77	3.4	42.76	7.2
10%ZnO	37.49	36.15	51.35	9.0	46.22	6.8	86.4	51.35	3.3	41.56	6.8
15%ZnO	37.98	35.01	40.78	5.0	40.78	5.4	69.2	40.78	2.6	33.05	4.3
20%ZnO	37.31	31.74	33.82	4.0	32.25	2.3	29.4	33.82	1.7	21.38	1.8

Preprints (www.preprints.org) | NOT PEER-REVIEWED | Posted: 1 October 2020 doi:10.20944/preprints202010.0026.v1

The mean crystallite size values estimated using the *UDM*, *UDSM*, and *UDEDM* models are virtually identical, signifying that the inclusion of strain in the altered formulae of W–H method has inconsequential impact on the average (D) value. Yet, the average crystallite sizes estimated using Scherrer's and W–H methods exhibit little disparity that can be ascribed to variation in particle size distribution averaging [39]. However, the data shows larger crystallite size for some of the samples by all Williamson- Hall models, still our data agree with previous investigations [44] that reported such convergence in the crystallite size results. All the ε and σ values obtained employing all the Williamson Hall models change proportional to the crystallite size in agreement with previously reported data [39]. When matching up the data obtained by the three models, it can be observed that there is a variation between the parameters obtained by *UDM* and the other two models confirming the anisotropic character of the nanoparticles [39]. This finding may support the change in the preferred orientation [37] as discussed earlier.

3.4. Morphological investigations:

The SEM images of the prepared nanocomposites are depicted in Fig. 3 (a – d). The 5 %ZnO sample (Fig. 3 a) reveals a blend of spherical and hexagonal particles with a size distribution 60 – 80 nm. In the 10 % and 15 %ZnO specimens' images (Fig. 3 b – c), the nanoparticles are transformed into fused oval shapes with size distribution 40 – 80 nm. In the 20 % ZnO sample the nanoparticles are turning into more hexagonal shape with less fusion and reduced size. The decrease in particles size of the highest Ti ratio sample may be attributed to the substitution of the Zn^{2+} (74 pm) with smaller radius Ti^{4+} (64 pm) [45]. Size distributions from SEM images are shown in Fig. 4.

Preprints (www.preprints.org) | NOT PEER-REVIEWED | Posted: 1 October 2020 doi:10.20944/preprints202010.0026.v1

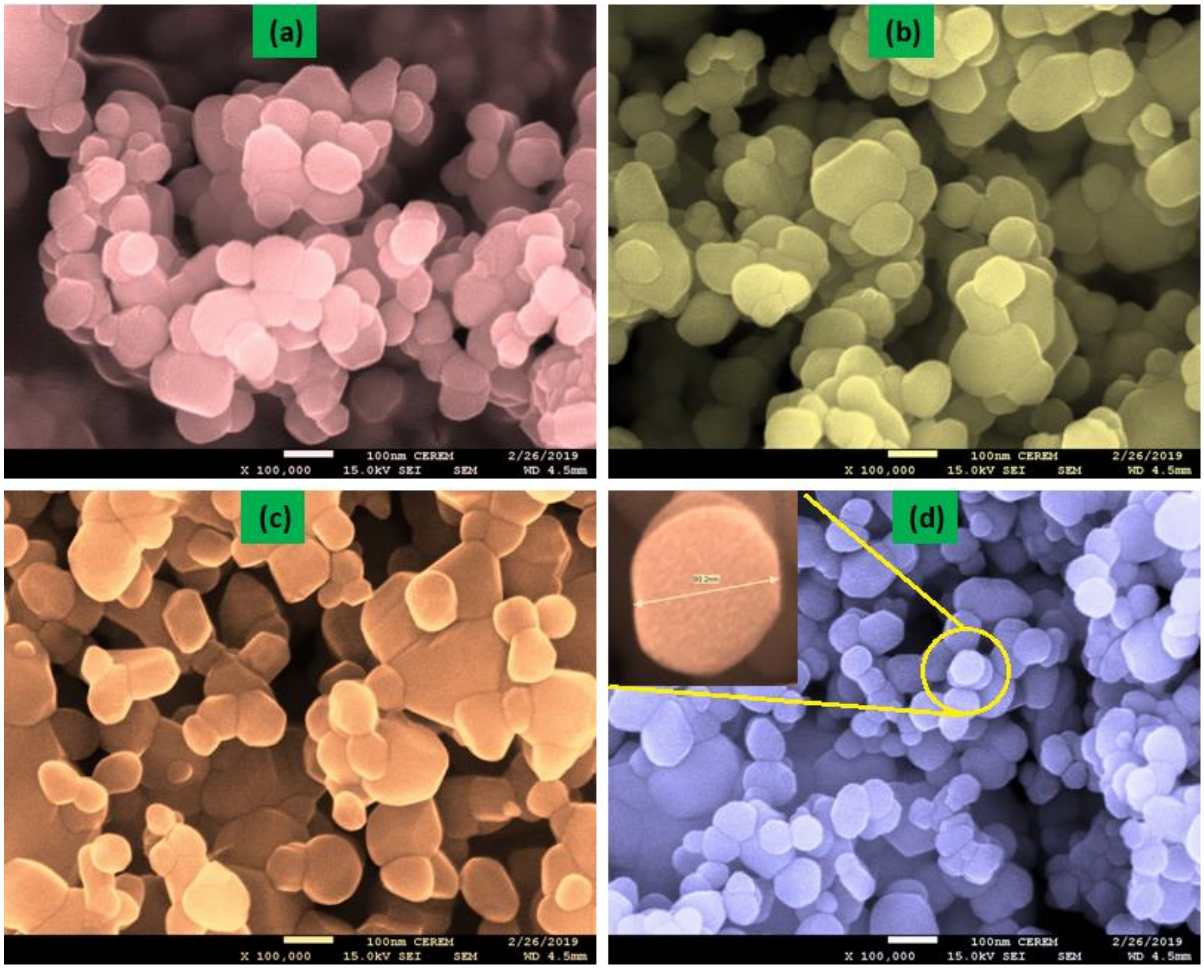

Fig. 3: SEM of 5 %ZnO (a), 10 %ZnO (b), 15 %ZnO (c) and 20 %ZnO (d)

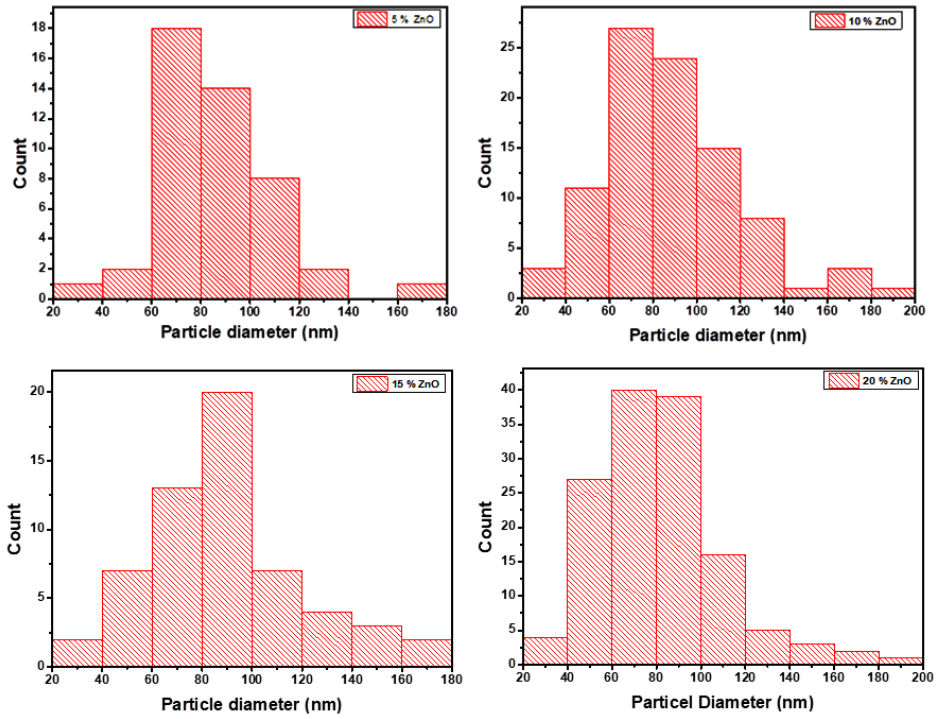

Fig. 4: Particle size distribution of samples from SEM images

Preprints (www.preprints.org) | NOT PEER-REVIEWED | Posted: 1 October 2020 doi:10.20944/preprints202010.0026.v1

3.5. Optical properties and band gap determination:

To optical properties the TiO_2/ZnO nanocomposites with varying Ti percentage were probed by UV–visible and their respective spectra are shown in Fig. 5. The graph reveals a maximum absorption at 373, 373, 369 and 370 nm for the 5%ZnO, 10%ZnO, 15%ZnO and 20%ZnO respectively. The band gap energy (E_g)was estimated from the$(\alpha hv)^2$ versus hv graph (Fig. 6) using the Tauc equation [46]:

$$(\alpha hv)^{1/2} = A(hv - E_g) \qquad (12)$$

where *h*, ν, α and E_g stand for; the Planck's constant, frequency, absorption coefficient and the band gap energy respectively, whereas A is a proportionality constant, and *n* designates the nature of electron transition (for directly allowed transitions, n = 1/2). The energy band gap values of were found to be 3.218, 3.212, 3.227 and 3.237eV the 5 %ZnO, 10 %ZnO, 15 %ZnO and 20%ZnO samples respectively. The E_g of the nanocomposites make them a promising candidates for different photo-applications [47,48]. During the doping process and the Ti^{4+} ions replacement of Zn^{2+}ions at substitution sites [49] an increase in the number of the free charge carriers prevails which considerably distresses low energy excitations. Such a situation may lead to the semiconductor's conduction band Fermi level expansion and a consequent optical band gap widening, in accordance with the Burstein–Moss shift [50,51]. Analogous blue shift phenomenon of optical band gaps in Ti-doped ZnO films [34,52] and Ti-doped ZnO nanoparticles [53] have been reported earlier.

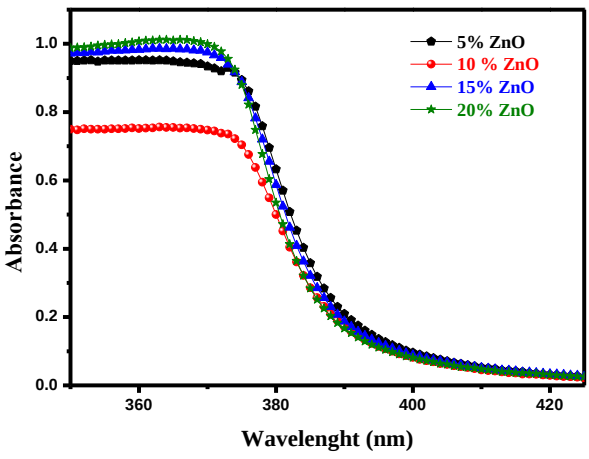

Fig. 5: UV-Vis absorbance of TiO_2/ZnO nanocomposites

Preprints (www.preprints.org) | NOT PEER-REVIEWED | Posted: 1 October 2020 doi:10.20944/preprints202010.0026.v1

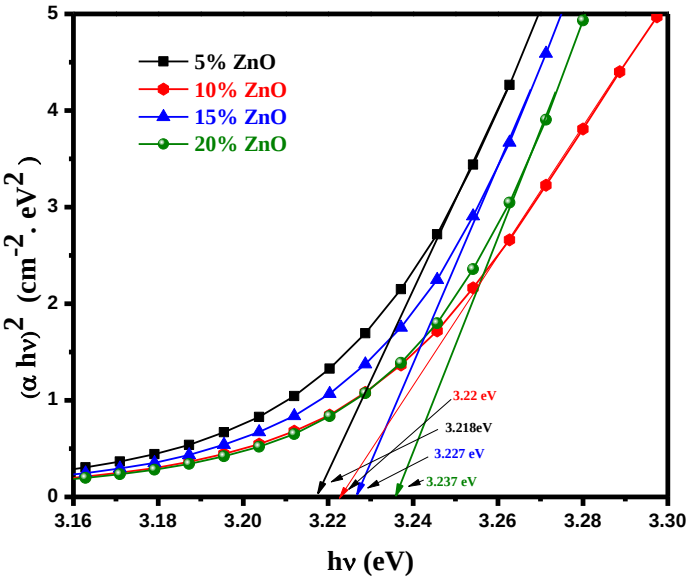

Fig. 6: The band gap energy of TiO_2/ZnO nanocomposites

3.6. Photocatalytic activity of nanocomposites

The photocatalytic performance of as-synthesized nanocomposites was assessed by the decomposition of RhB dye under visible light illumination. As presented in Fig 7a. RhB dye has achieved poor photocatalytic activity in the presence of pure ZnO under visible light illumination, which was a result of the fast recombination of photogenerated electron−hole pairs [54]. On the other hand, the TiO_2/ZnO samples demonstrated improved photocatalytic performance (Fig. 7b). With increasing TiO_2 content, the photodegradation competence of the nanocomposites has markedly improved [55]. Among them, 20% doped ZnO exemplified the best performance with a dye photo-degradation rate of 97% within 180 min (Fig. 8a). The kinetics of the photodegradation was greatly fits the first order kinetics as indicated by the linear ln C_0/C_t vs t plots (Fig. 8b) and the regression values ($R^2 \approx 1.0$) [56]. The rate constant and half-life values (Table 3) clearly confirm the highest photodegradation capacity of the 20% doped ZnO sample.

Preprints (www.preprints.org) | NOT PEER-REVIEWED | Posted: 1 October 2020 doi:10.20944/preprints202010.0026.v1

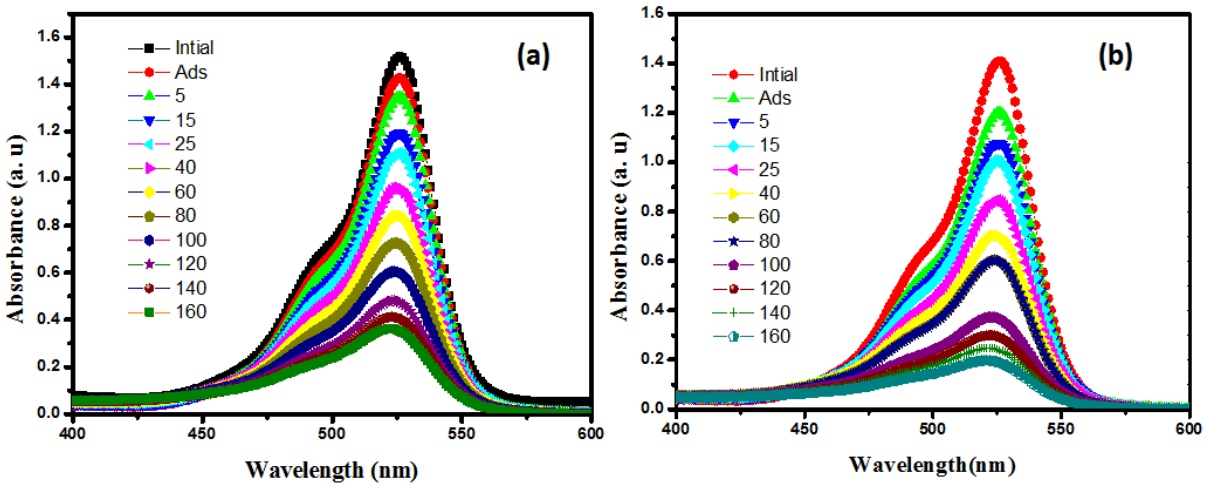

Fig. 7: RhB photodegradation by a) ZnO and b) 20% ZnO under visible light illumination

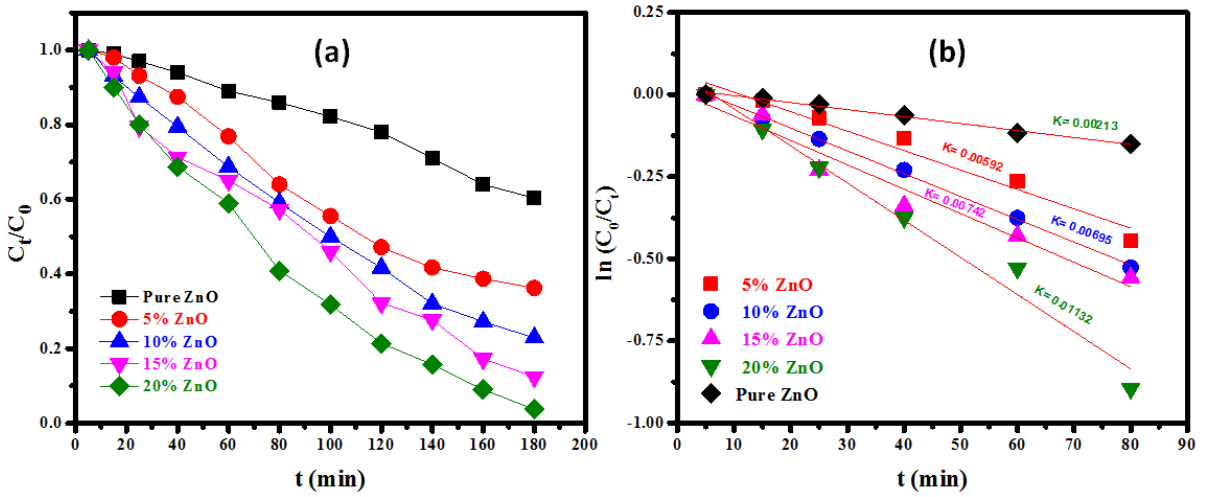

Fig. 8: a) Samples photodegradation performance and b) Kinetics of RhB photodegradation under visible light illumination

Table 3: Kinetics parameters of RhB degradation

Samples	k (min^{-1})	$t_{1/2}$	R^2	Degradation %
ZnO	0.00213	327	0.988	39.7
5 %ZnO	0.00592	117	0.957	63.8
10 %ZnO	0.00695	100	0.998	77.2
15 %ZnO	0.00742	93	0.952	87.5
20 %ZnO	0.01132	61	0.975	97.0

Preprints (www.preprints.org) | NOT PEER-REVIEWED | Posted: 1 October 2020 doi:10.20944/preprints202010.0026.v1

3.7. Mechanism of Photocatalysis:

Electrons get excited due to ultraviolet of visible light irradiation electrons and are then promoted from valence band (VB) to conduction band (CB) of ZnO NPs creating a positive holes (h^+) behind [57]. The powerful oxidizing $O_2^{-\bullet}$ resulting an electrons and an O_2 reaction do combine with hole (h^+) to generate the peroxide H_2O_2 (O_2+ 2 h^+ +2e^- →H_2O_2) that triggers chain reactions with electrons to the produce the active •OH radicals (H_2O_2 + e^- → OH^- +$^{\bullet}$OH). Similarly $^{\bullet}$OH can be generated from the h^+ reaction with surface adsorbed H_2O molecules [58]. The photodegradation reaction proceeds due to the continuous bouts on the organic dye by •OH radicals (R + $^{\bullet}$OH → R$^{\bullet\prime}$+ H_2O) or h^+ (R + h^+ → $R^{\bullet+}$ → degradation products [59]. Fig. 9 is a graphical description for a photodegradation scheme.

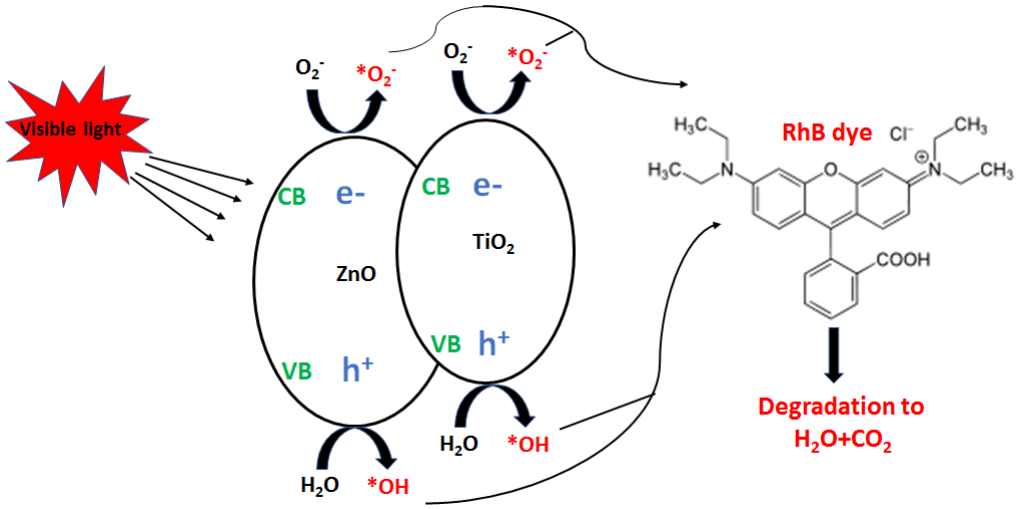

Fig. 9: Elucidation of RhB photodegradation

3.8. Influence of radicals' scavengers on the photocatalytic activity

Oxygen species are reactive radicals are usually involved in the photodegradation process. In order to verify the operative entities, the scavengers EDTA, isopropanol, silver nitrate and ascorbic acid are employed to monitor the effects of positive holes, hydroxyl radicals, electrons and superoxide radicals respectively on TiO_2/ZnO photo-composite. The photodegradation (C_t/C_0) percentage variation with scavengers is displayed in Fig. 10. It

Preprints (www.preprints.org) | NOT PEER-REVIEWED | Posted: 1 October 2020 doi:10.20944/preprints202010.0026.v1

can be seen that photodegradation yields are 10%, 5%, 15%, and 30% due to the addition of EDTA (h^+ scavenger) [60] and ASC ($\bullet O_2^-$ scavenger) [61] as compared to IPA (•OH scavenger) [61] and $AgNO_3$ (e^- scavenger) respectively. This implies that the h^+ [62] and $\bullet O_2^-$ [63] radicals have more contribution to the dye photodegradation compared to •OH and e^- that show less impact on the photodegradation process by the TiO_2/ZnO photocatalyst.

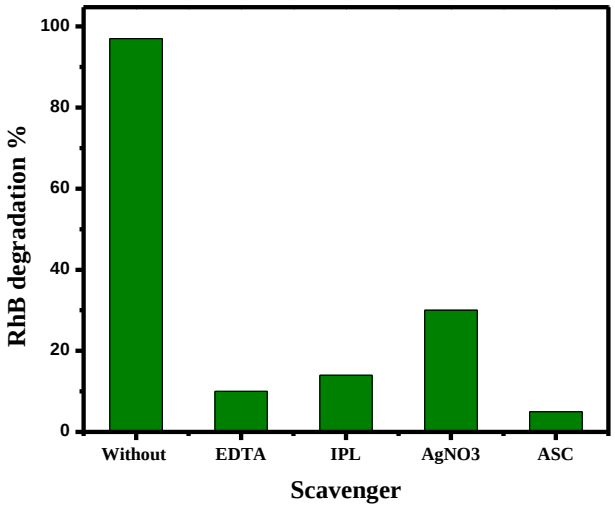

Fig. 10: Effects of radicals' scavengers of the RhB photodegradation percentage

Table 4 shows a comparison of the photocatalytic competence of 20%ZnO with other photocatalysts from literature. The data undoubtedly exhibit the higher performance of the photocatalyst to decolorize RhB in aqueous solutions.

Table. 4: Comparison of the 20 %ZnO photocatalytic activity with other photocatalysts

Photocatalyst	RhB dye	Degradation%	Ref.
300 mg 1% TiO_2@Rgo	30 mgL^{-1}	96	[64]
30 mg $ZnFe_2O_4$	10 mgL^{-1}	81	[65]
50 mg CdTe	10 mgL^{-1}	80	[66]
150 mg Cr-doped $SrTiO_3$	10 mgL^{-1}	77	[67]
50 mg Ag@Mn_xO_y	100 mgL^{-1}	91	[68]
100 mg Fe-TiO_2-SiC	5 mgL^{-1}	90	[69]
100 mg CdS	20 mgL^{-1}	70	[70]
50 mg 20%ZnO	100 mgL^{-1}	97	This work

4. Conclusion

The doping of ZnO with various percentage of TiO_2 has dramatically improved it is competent for the photocatalytic degradation of RhB dye under visible light illumination. The nanocomposites prepared via a facile ultra-sonication exhibited crystallite size reduction with the rutile TiO_2 phase's development as perceived from the XRD data. The optical properties revealed higher absorbance for the 20 %ZnO sample with a band gap energy of 3.23 eV. The 20 %ZnO showed enhanced photodegradation activity that followed the pseudo-first-order kinetics with 0.01132 min^{-1} rate constant. The scavengers tests indicated that the h^+ and $\bullet O_2^-$ are the most effective species involved in the dye degradation. Based on the results presented in this research, ZnO doped with TiO_2 has the potential for use as an efficient photocatalyst for polluting organic dyes in aqueous discharges.

Acknowledgments

The authors extend their appreciation to the Deputyship for Research& Innovation, Ministry of Education in Saudi Arabia for funding this research work through the project number 510.

5. References

1. Arul, K.T.; Manikandan, E.; Murmu, P.; Kennedy, J.; Henini, M. Enhanced magnetic properties of polymer-magnetic nanostructures synthesized by ultrasonication. *Journal of Alloys and Compounds* **2017**, *720*, 395-400.
2. Armstrong, G. An introduction to polymer nanocomposites. *European Journal of Physics* **2015**, *36*, 063001.
3. Sundarrajan, P.; Eswaran, P.; Marimuthu, A.; Subhadra, L.B.; Kannaiyan, P. One pot synthesis and characterization of alginate stabilized semiconductor nanoparticles. *Bulletin of the Korean Chemical Society* **2012**, *33*, 3218-3224.
4. Goda, K.; Sreekala, M.S.; Malhotra, S.K.; Joseph, K.; Thomas, S. Advances in polymer composites: biocomposites–state of the art, new challenges, and opportunities. *Edited by Sabu Thomas, Kuruvilla Joseph, SK Malhotra* **2014**.
5. Bauermann, L.P.; del Campo, A.; Bill, J.; Aldinger, F. Heterogeneous nucleation of ZnO using gelatin as the organic matrix. *Chemistry of Materials* **2006**, *18*, 2016-2020.

6. Tseng, Y.-H.; Lin, H.-Y.; Liu, M.-H.; Chen, Y.-F.; Mou, C.-Y. Biomimetic synthesis of nacrelike faceted mesocrystals of ZnO− gelatin composite. *The Journal of Physical Chemistry C* **2009**, *113*, 18053-18061.
7. Parani, S.; Pandian, K.; Oluwafemi, O.S. Gelatin stabilization of quantum dots for improved stability and biocompatibility. *International journal of biological macromolecules* **2018**, *107*, 635-641.
8. Zhang, D.; Yang, H. Gelatin-stabilized copper nanoparticles: synthesis, morphology, and their surface-enhanced Raman scattering properties. *Physica B: Condensed Matter* **2013**, *415*, 44-48.
9. Zak, A.K.; Majid, W.A.; Darroudi, M.; Yousefi, R. Synthesis and characterization of ZnO nanoparticles prepared in gelatin media. *Materials Letters* **2011**, *65*, 70-73.
10. Hyam, R.S.; Bhosale, R.K.; Lee, W.; Han, S.; Hannoyer, B.; Ogale, S.B. Room temperature synthesis of rutile TiO2 hierarchical nanoneedle flower morphology for dye sensitized solar cell. *Journal of nanoscience and nanotechnology* **2010**, *10*, 5894-5898.
11. Rajkumar, N.; Kanmani, S.; Ramachandran, K. Performance of dye-sensitized solar cell based on TiO2: ZnO nanocomposites. *Advanced Science Letters* **2011**, *4*, 627-633.
12. Marci, G.; Augugliaro, V.; López-Muñoz, M.J.; Martín, C.; Palmisano, L.; Rives, V.; Schiavello, M.; Tilley, R.J.; Venezia, A.M. Preparation characterization and photocatalytic activity of polycrystalline ZnO/TiO2 systems. 1. Surface and bulk characterization. *The Journal of Physical Chemistry B* **2001**, *105*, 1026-1032.
13. Kandavelu, V.; Kastien, H.; Thampi, K.R. Photocatalytic degradation of isothiazolin-3-ones in water and emulsion paints containing nanocrystalline TiO2 and ZnO catalysts. *Applied Catalysis B: Environmental* **2004**, *48*, 101-111.
14. Lin, S.-S.; Huang, J.-L.; Lii, D.-F. The effect of thickness on the properties of Ti-doped ZnO films by simultaneous rf and dc magnetron sputtering. *Surface and coatings Technology* **2005**, *190*, 372-377.
15. WON, T.H.; RYU, J.Y.; CHOI, W.C.; KIM, S.W.; PARK, S.H.; CHOI, H.H.; LEE, M.K. Investigation on sensing properties of ZnO-based thin film sensors for trimethylamine gas. *Sensors and materials* **1999**, *11*, 257-267.
16. Wang, C.; Xu, B.-Q.; Wang, X.; Zhao, J. Preparation and photocatalytic activity of ZnO/TiO2/SnO2 mixture. *Journal of solid state chemistry* **2005**, *178*, 3500-3506.
17. Wu, W.; Cai, Y.; Chen, J.; Shen, S.; Martin, A.; Wen, L. Preparation and properties of composite particles made by nano zinc oxide coated with titanium dioxide. *Journal of Materials Science* **2006**, *41*, 5845-5850.
18. Tai, W.-P.; Kim, J.-G.; Oh, J.-H. Humidity sensitive properties of nanostructured Al-doped ZnO: TiO2 thin films. *Sensors and Actuators B: Chemical* **2003**, *96*, 477-481.
19. Barreca, D.; Comini, E.; Ferrucci, A.P.; Gasparotto, A.; Maccato, C.; Maragno, C.; Sberveglieri, G.; Tondello, E. First example of ZnO− TiO2 nanocomposites by chemical vapor deposition: structure, morphology, composition, and gas sensing performances. *Chemistry of Materials* **2007**, *19*, 5642-5649.
20. Houšková, V.; Štengl, V.; Bakardjieva, S.; Murafa, N. Photoactive materials prepared by homogeneous hydrolysis with thioacetamide: Part 2—TiO2/ZnO nanocomposites. *Journal of Physics and Chemistry of Solids* **2008**, *69*, 1623-1631.
21. Taha, K.K.; Modwi, A.; Elamin, M.; Arasheed, R.; AL-Fahad, A.J.; Albutairi, I.; Alfaify, M.; Anojaidi, K.; Algethami, F.K.; Bagabas, A. Impact of Hibiscus extract on the structural and activity of sonochemically fabricated ZnO nanoparticles. *Journal of Photochemistry and Photobiology A: Chemistry* **2020**, *390*, 112263.
22. Munawar, T.; Yasmeen, S.; Hasan, M.; Mahmood, K.; Hussain, A.; Ali, A.; Arshad, M.; Iqbal, F. Novel tri-phase heterostructured ZnO–Yb2O3–Pr2O3

nanocomposite; structural, optical, photocatalytic and antibacterial studies. *Ceramics International* **2020**.

23. Siva Vijayakumar, T.; Karthikeyeni, S.; Vasanth, S.; Ganesh, A.; Bupesh, G.; Ramesh, R.; Manimegalai, M.; Subramanian, P. Synthesis of silver-doped zinc oxide nanocomposite by pulse mode ultrasonication and its characterization studies. *Journal of Nanoscience* **2013**, *2013*.
24. Verma, R.; Gangwar, J.; Srivastava, A.K. Multiphase TiO 2 nanostructures: a review of efficient synthesis, growth mechanism, probing capabilities, and applications in bio-safety and health. *RSC Advances* **2017**, *7*, 44199-44224.
25. Gao, Q.; Wu, X.; Fan, Y. The effect of iron ions on the anatase–rutile phase transformation of titania (TiO2) in mica–titania pigments. *Dyes and Pigments* **2012**, *95*, 96-101.
26. Prasad, K.; Pinjari, D.; Pandit, A.; Mhaske, S. Synthesis of titanium dioxide by ultrasound assisted sol–gel technique: effect of amplitude (power density) variation. *Ultrasonics sonochemistry* **2010**, *17*, 697-703.
27. Bueno, C.; Maestre, D.; Díaz, T.; Juárez, H.; Pacio, M.; Cremades, A.; Piqueras, J. High-yield growth of Ti doped ZnO nano-and microstructures by a vapor-solid method. *Journal of Alloys and Compounds* **2017**, *726*, 201-208.
28. Bidier, S.A.; Hashim, M.; Al-Diabat, A.M.; Bououdina, M. Effect of growth time on Ti-doped ZnO nanorods prepared by low-temperature chemical bath deposition. *Physica E: Low-dimensional Systems and Nanostructures* **2017**, *88*, 169-173.
29. Modwi, A.; Abbo, M.; Hassan, E.; Taha, K.; Khezami, L.; Houas, A. INFLUENCE OF ANNEALING TEMPERATURE ON THE PROPERTIES OF ZnO SYNTHESIZED VIA 2.3. DIHYDROXYSUCCINIC ACID USING FLASH SOL-GEL METHOD. *Journal of Ovonic research* **2016**, *12*.
30. Jadhav, N.H.; Shinde, D.R.; Sakate, S.S.; Rasal, N.K.; Pawar, R.A. Ti (IV) doping: An effective strategy to boost Lewis acidic performance of ZnO catalyst in fluorescein dye synthesis. *Catalysis Communications* **2019**, *120*, 17-22.
31. Muthukumaran, S. Effect of solvents on the structural, optical and morphological properties of Zn 0.96 Cu 0.04 O nanoparticles. *Journal of Materials Science: Materials in Electronics* **2013**, *24*, 4050-4059.
32. Lupan, O.; Pauporté, T.; Chow, L.; Viana, B.; Pellé, F.; Ono, L.; Cuenya, B.R.; Heinrich, H. Effects of annealing on properties of ZnO thin films prepared by electrochemical deposition in chloride medium. *Applied Surface Science* **2010**, *256*, 1895-1907.
33. Modwi, A.; Khezami, L.; Taha, K.K.; Houas, A. Structural, surface area and FTIR characterization of Zn 0.95− x Cu 0.05 Fe 0.0 x O nanocomposites prepared via sol–gel method. *Journal of Materials Science: Materials in Electronics* **2018**, *29*, 2184-2192.
34. Zhong, Z.; Zhang, T. Microstructure and optoelectronic properties of titanium-doped ZnO thin films prepared by magnetron sputtering. *Materials Letters* **2013**, *96*, 237-239.
35. Chen, H.; Ding, J.; Shi, F.; Li, Y.; Guo, W. Optical properties of Ti-doped ZnO films synthesized via magnetron sputtering. *Journal of Alloys and Compounds* **2012**, *534*, 59-63.
36. Bokhimi, X.; Morales, A.; Pedraza, F. Crystallography and crystallite morphology of rutile synthesized at low temperature. *Journal of solid state chemistry* **2002**, *169*, 176-181.
37. Wang, J.; Kim, J.; Bardwell, J.; Brown, J.; Stokes, E.; Kuo, H.; Hunter, G. State-of-the-Art Program on Compound Semiconductorss 47 (SOTAPOCS 47) and Wide Bandgap Semiconductor Materials and Devices 8.

38. Taha, K.K.; Modwi, A.; Elamin, M.; Arasheed, R.; AL-Fahad, A.J.; Albutairi, I.; Alfaify, M.; Anojaidi, K.; Algethami, F.K.; Bagabas, A. Impact of Hibiscus Extract on the Structural and Activity of Sonochemically Fabricated ZnO Nanoparticles. *Journal of Photochemistry and Photobiology A: Chemistry* **2019**, 112263.
39. Zak, A.K.; Majid, W.A.; Abrishami, M.E.; Yousefi, R. X-ray analysis of ZnO nanoparticles by Williamson–Hall and size–strain plot methods. *Solid State Sciences* **2011**, *13*, 251-256.
40. Pandiyarajan, T.; Karthikeyan, B. Cr doping induced structural, phonon and excitonic properties of ZnO nanoparticles. *Journal of Nanoparticle Research* **2012**, *14*, 647.
41. Bindu, P.; Thomas, S. Estimation of lattice strain in ZnO nanoparticles: X-ray peak profile analysis. *Journal of Theoretical and Applied Physics* **2014**, *8*, 123-134.
42. Ungár, T. Characterization of nanocrystalline materials by X-ray line profile analysis. *Journal of materials science* **2007**, *42*, 1584-1593.
43. Brandstetter, S.; Derlet, P.; Van Petegem, S.; Van Swygenhoven, H. Williamson–Hall anisotropy in nanocrystalline metals: X-ray diffraction experiments and atomistic simulations. *Acta Materialia* **2008**, *56*, 165-176.
44. Mote, V.; Purushotham, Y.; Dole, B. Williamson-Hall analysis in estimation of lattice strain in nanometer-sized ZnO particles. *Journal of Theoretical and Applied Physics* **2012**, *6*, 6.
45. Li, W.; Liang, R.; Hu, A.; Huang, Z.; Zhou, Y.N. Generation of oxygen vacancies in visible light activated one-dimensional iodine TiO 2 photocatalysts. *RSC Advances* **2014**, *4*, 36959-36966.
46. Tauc, J. Optical properties and electronic structure of amorphous Ge and Si. *Materials Research Bulletin* **1968**, *3*, 37-46.
47. Han, Z.; Ren, L.; Cui, Z.; Chen, C.; Pan, H.; Chen, J. Ag/ZnO flower heterostructures as a visible-light driven photocatalyst via surface plasmon resonance. *Applied Catalysis B: Environmental* **2012**, *126*, 298-305.
48. Wang, S.; Yu, Y.; Zuo, Y.; Li, C.; Yang, J.; Lu, C. Synthesis and photocatalysis of hierarchical heteroassemblies of ZnO branched nanorod arrays on Ag core nanowires. *Nanoscale* **2012**, *4*, 5895-5901.
49. Lu, Y.-M.; Chang, C.-M.; Tsai, S.-I.; Wey, T.-S. Improving the conductance of ZnO thin films by doping with Ti. *Thin Solid Films* **2004**, *447*, 56-60.
50. Jun, M.-C.; Park, S.-U.; Koh, J.-H. Comparative studies of Al-doped ZnO and Ga-doped ZnO transparent conducting oxide thin films. *Nanoscale research letters* **2012**, *7*, 639.
51. Benzarouk, H.; Drici, A.; Mekhnache, M.; Amara, A.; Guerioune, M.; Bernède, J.C.; Bendjffal, H. Effect of different dopant elements (Al, Mg and Ni) on microstructural, optical and electrochemical properties of ZnO thin films deposited by spray pyrolysis (SP). *Superlattices and Microstructures* **2012**, *52*, 594-604.
52. Ye, Z.-Y.; Lu, H.-L.; Geng, Y.; Gu, Y.-Z.; Xie, Z.-Y.; Zhang, Y.; Sun, Q.-Q.; Ding, S.-J.; Zhang, D.W. Structural, electrical, and optical properties of Ti-doped ZnO films fabricated by atomic layer deposition. *Nanoscale research letters* **2013**, *8*, 108.
53. Naeem, M.; Qaseem, S.; Gul, I.; Maqsood, A. Study of active surface defects in Ti doped ZnO nanoparticles. *Journal of applied physics* **2010**, *107*, 124303.
54. Saravanan, R.; Gupta, V.; Mosquera, E.; Gracia, F. Preparation and characterization of V2O5/ZnO nanocomposite system for photocatalytic application. *Journal of Molecular Liquids* **2014**, *198*, 409-412.
55. Wang, Y.; Zheng, Y.-Z.; Lu, S.; Tao, X.; Che, Y.; Chen, J.-F. Visible-light-responsive TiO2-coated ZnO: I nanorod array films with enhanced

photoelectrochemical and photocatalytic performance. *ACS applied materials & interfaces* **2015**, *7*, 6093-6101.

56. Hidalgo, M.; Pessoa, C.; Fernandez, E.; Cardenas, A. Comparative determination of photodegradation kinetics of quinolones. *Journal of Photochemistry and Photobiology A: Chemistry* **1993**, *73*, 135-138.
57. Wang, J.; Shen, H.; Dai, X.; Li, C.; Shi, W.; Yan, Y. Graphene oxide as solid-state electron mediator enhanced photocatalytic activities of GO-Ag3PO4/Bi2O3 Z-scheme photocatalyst efficiently by visible-light driven. *Materials Technology* **2018**, *33*, 421-432.
58. Wu, G.; Xing, W. Fabrication of ternary visible-light-driven semiconductor photocatalyst and its effective photocatalytic performance. *Materials Technology* **2018**, 1-9.
59. Houas, A.; Lachheb, H.; Ksibi, M.; Elaloui, E.; Guillard, C.; Herrmann, J.-M. Photocatalytic degradation pathway of methylene blue in water. *Applied Catalysis B: Environmental* **2001**, *31*, 145-157.
60. Zhang, H.; Zong, R.; Zhu, Y. Photocorrosion inhibition and photoactivity enhancement for zinc oxide via hybridization with monolayer polyaniline. *The Journal of Physical Chemistry C* **2009**, *113*, 4605-4611.
61. Lv, J.; Dai, K.; Zhang, J.; Liu, Q.; Liang, C.; Zhu, G. Facile constructing novel 2D porous g-C3N4/BiOBr hybrid with enhanced visible-light-driven photocatalytic activity. *Separation and Purification Technology* **2017**, *178*, 6-17.
62. Kadam, A.; Bhopate, D.; Kondalkar, V.; Majhi, S.; Bathula, C.; Tran, A.-V.; Lee, S.-W. Facile synthesis of Ag-ZnO core–shell nanostructures with enhanced photocatalytic activity. *Journal of Industrial and Engineering Chemistry* **2018**, *61*, 78-86.
63. Upreti, A.R.; Li, Y.; Khadgi, N.; Naraginti, S.; Zhang, C. Efficient visible light photocatalytic degradation of 17α-ethinyl estradiol by a multifunctional Ag–AgCl/ZnFe 2 O 4 magnetic nanocomposite. *RSC Advances* **2016**, *6*, 32761-32769.
64. Ali, M.H.; Al-Afify, A.D.; Goher, M.E. Preparation and characterization of graphene–TiO2 nanocomposite for enhanced photodegradation of Rhodamine-B dye. *The Egyptian Journal of Aquatic Research* **2018**, *44*, 263-270.
65. Golsefidi, M.A.; Abrodi, M.; Abbasi, Z.; Dashtbozorg, A.; Rostami, M.E.; Ebadi, M. Hydrothermal method for synthesizing ZnFe 2 O 4 nanoparticles, photo-degradation of Rhodamine B by ZnFe 2 O 4 and thermal stable PS-based nanocomposite. *Journal of Materials Science: Materials in Electronics* **2016**, *27*, 8654-8660.
66. Golsefidi, M.A.; Ramandi, M.F.; Shahkooie, M.A.K. Facile synthesis of CdTe nanoparticles and photo-degradation of Rhodamine B and methyl orange. *Journal of Materials Science: Materials in Electronics* **2016**, *27*, 12100-12105.
67. Rahman, Q.I.; Ahmad, M.; Mehta, S. Hydrothermal synthesis of Cr-doped SrTiO 3 nanoparticles for rhodamine-B dye degradation under visible light illumination. *Colloid and Polymer Science* **2017**, *295*, 933-937.
68. Saeed, M.; Ahmad, A.; Boddula, R.; ul Haq, A.; Azhar, A. Ag@ Mn x O y: an effective catalyst for photo-degradation of rhodamine B dye. *Environmental chemistry letters* **2018**, *16*, 287-294.
69. Kim, T.H.; Gómez-Solís, C.; Moctezuma, E.; Lee, S.W. Sonochemical synthesis of Fe–TiO 2–SiC composite for degradation of rhodamine B under solar simulator. *Research on Chemical Intermediates* **2014**, *40*, 1595-1605.
70. Song, L.; Li, Y.; Zhang, S. Sonocatalytic degradation of rhodamine B in presence of CdS. *Environmental Science and Pollution Research* **2018**, *25*, 10714-10719.